American Mineralogist, Volume 102, pages 900–908, 2017

Ca $L_{2,3}$-edge near edge X-ray absorption fine structure of tricalcium aluminate, gypsum, and calcium (sulfo)aluminate hydrates

Guoqing Geng[1,*], Rupert J. Myers[1,4], Arthur L.D. Kilcoyne[2], Juyoung Ha[3], and Paulo J.M. Monteiro[1,2]

[1]Department of Civil and Environmental Engineering, University of California, Berkeley, California 94720, U.S.A.
[2]Advanced Light Source, Lawrence Berkeley National Laboratory, Berkeley, California 94720, U.S.A.
[3]School of Environmental and Sustainability Sciences, Kean University, Union, New Jersey 07083, U.S.A.
[4]School of Forestry & Environmental Studies, Yale University, 195 Prospect Street, New Haven, Connecticut 06511, U.S.A.

Abstract

Tricalcium aluminate (cement clinker phase), gypsum, katoite, ettringite, and calcium monosulfoaluminate hydrate (abbreviated as kuzelite) are the major minerals in the hydration reaction of tricalcium aluminate in the presence of gypsum and have critical impacts on the kinetics and thermodynamics of early-age cement hydration mechanisms. Here, spectroscopic analysis of these minerals is conducted using scanning transmission X-ray microscopy (STXM). Their Ca $L_{2,3}$-edge near edge X-ray absorption fine structure (NEXAFS) spectra are measured and correlated to the known Ca coordination environments. The results indicate that these minerals have unique Ca environments that can be differentiated from one another based on the intensities and positions of the absorption peaks at 346.5–348.5 and 350.5–351.5 eV. It is concluded that Ca in tricalcium aluminate (cubic and orthorhombic polymorphs) and katoite is in cubic-like coordination with negative 10Dq, whereas Ca is in an octahedral-like coordination with positive 10Dq in ettringite, gypsum, and kuzelite. For tricalcium aluminate, the Ca atoms in both polymorphs are in similar chemical environments with slightly more distortion in the orthorhombic polymorph. As a common issue in STXM experiments, absorption saturation of NEXAFS spectra is also investigated. It is demonstrated that the optical density difference between pre- and post-edge absorption levels provides a reliable indication of the sample thickness in the systems studied. The present work provides a reference for the STXM study of the calcium (sulfo)aluminate reactions in cement hydration and natural aqueous environments, and in the former case, provides a more complete understanding of a system that may serve as a low-C alternative to Portland cement.

Keywords: Tricalcium aluminate, calcium aluminate hydrate, calcium sulfoaluminate hydrate, STXM, NEXAFS, Ca $L_{2,3}$-edge, absorption saturation

Introduction

Calcium (sulfo)aluminate hydrates are found in geological formations (Bell and Rossman 1992; Nelson 1982), wet near-surface environments (Puppala et al. 2005; van Aardt and Visser 1977), and complex composite materials such as hydrated Portland cement (PC) (Taylor 1997; Mehta and Monteiro 2014). Recent studies suggest that heavy metal oxyanions, such as chromate (Hashem and Amin 2014), arsenate (Sasaki et al. 2014), and selenate (Baur and Johnson 2003), can be immobilized using calcium (sulfo)aluminate hydrates, e.g., ettringite (Chrysochoou and Dermatas 2006; Zhou et al. 2006; Hillier et al. 2007), as these elements can be directly substituted into the structures of these minerals. The substitution extent of heavy metal oxyanions has been shown to depend on the coordination environment of Ca with respect to sulfate. It has also been suggested that the coordination environment of Ca is a critical parameter in determining the reactivity of minerals (Davidovits 1994; Skibsted et al. 1993; Black et al. 2003). The Ca coordination symmetry of many natural and synthetic solid phases has been studied by Ca $L_{2,3}$-edge NEXAFS (Solomon et al. 2012; Ha et al. 2012; Jackson et al. 2013; Geng et al. 2015; Fleet and Liu 2009). The peak structures and separations at the absorption edges are affected by the crystal field splitting and spin-orbit effects (Stöhr 2013). Nanometer-resolved identification of Ca coordination environments in complex composite materials (e.g., hydrated cement) has been reported but seems challenging due to the lack of direct links between NEXAFS spectra and coordination configurations (Solomon et al. 2012; Jackson et al. 2013). The efficient assignment of spectra to mineral phases greatly relies on understanding the reference spectra of known minerals and semi-empirical prediction of coordination environment from the spectra details.

Scanning transmission X-ray microscopy (STXM) combines spatially resolved measurements with X-rays of tunable energy at synchrotron radiation facilities (Warwick et al. 2002; Kilcoyne et al. 2003). The bonding and coordination environments of Ca in calcium (sulfo)aluminate hydrates intermixed on the nano- and

* E-mail: guoqinggeng1989@gmail.com

0003-004X/17/0004–900$05.00/DOI: http://dx.doi.org/10.2138/am-2017-5670

microscales can be spatially determined by STXM using coupled near edge X-ray absorption fine structure (NEXAFS) measurements (Stöhr 2013). This technique has gained significant interest in geology (Wan et al. 2007), environmental and material research applications (Chen et al. 2014), photovoltaics (McNeill et al. 2008), and cosmological chemistry (Sandford et al. 2006). Cement hydration systems have submicrometer chemical and structural heterogeneities that greatly influence their macroscopic performances, e.g., rheology, hydration heat release and volumetric stability. STXM provides a powerful analytical tool for measuring both spectroscopic and spatial information down to the micro- or nanometer scales for cementitious materials; however, collecting reference spectra of cement-based minerals is critical for analyzing the spatially resolved spectroscopic data.

Tricalcium aluminate ($3CaO{\cdot}Al_2O_3$, abbreviated as C_3A) is a clinker mineral whose hydration determines the early age performance of fresh concrete mixtures. It is cubic (C_3A_{cub}) when the Na_2O mass content is less than 1.9 wt% and orthorhombic (C_3A_{orth}) when the Na_2O doping is between 3.5 and 4.2 wt% (Barnes and Bensted 2002). Its direct reaction with water rapidly forms metastable calcium aluminate hydrates, which quickly become katoite ($3CaO{\cdot}Al_2O_3{\cdot}6H_2O$, a garnet structure type mineral). In the presence of gypsum ($CaSO_4{\cdot}2H_2O$), the hydration speed is adjusted by the slow formation of ettringite ($3CaO{\cdot}Al_2O_3{\cdot}3CaSO_4{\cdot}32H_2O$), which is later transformed into calcium monosulfoaluminate hydrate, i.e., kuzelite ($3CaO{\cdot}Al_2O_3{\cdot}CaSO_4{\cdot}12H_2O$) through reaction with remnant C_3A after the gypsum is completely consumed (Barnes and Bensted 2002). In this project, STXM is used to collect the reference Ca $L_{2,3}$-edge NEXAFS spectra of several calcium (sulfo)aluminate hydrate mineral phases. The correlations between the spectral features and Ca coordination environments are discussed. The influence of the absorption saturation on the correct interpretation of the Ca $L_{2,3}$-edge NEXAFS spectra is also studied. This work provides reference spectra for the STXM study of calcium (sulfo)aluminate reaction systems in cement hydration and natural aqueous environments.

Ca $L_{2,3}$-edge NEXAFS theory

The crystal field splitting of d^0 compounds such as Ca^{2+} has been investigated experimentally and theoretically (Fig. 1) to understand the link between coordination symmetry and near-edge adsorption fine structure (de Groot et al. 1990; Burns 1993; Albright et al. 2013). The lowest unoccupied molecular orbitals (LUMOs) in the CaO_x complex are t_{2g} and e_g. They are close in energy but distinct in symmetry. The t_{2g} state is mainly composed of d_{xy}, d_{yz}, and d_{xz} orbitals and therefore has the same symmetry as these orbitals, whereas e_g is mainly composed of d_{z2} and d_{x2-y2} orbitals. In the isolated Ca^{2+} ion, the t_{2g} and e_g states share the same energy, but when approached by coordinating O atoms, their energies become significantly different. The t_{2g} state is at a higher energy than the e_g state when Ca coordination is in cubic symmetry whereas the opposite is true for octahedral symmetry. Therefore, the energy gap (e_g-t_{2g}), equivalently termed $10Dq$, is negative for cubic symmetry and positive for octahedral symmetry. A typical Ca $L_{2,3}$-edge NEXAFS spectra has two major peaks (a_2 and b_2), two minor peaks (a_1 and b_1), and several leading peaks (1, 2 possibly). The spin-orbital interaction splits the Ca $L_{2,3}$-edge

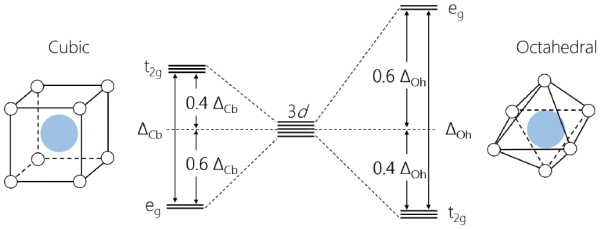

Figure 1. Representation of the crystal field splitting of 3d orbitals in cubic and octahedral coordination states in Ca^{2+}. Here, the central atoms (solid blue circles) are Ca and the coordinated atoms (hollow circles) are oxygen. Descriptions of the various parameters depicted are described in the text. Adapted from Burns (1993). (Color online.)

NEXAFS spectra into two doublets. The lower-energy doublet (a_1 and a_2) corresponds to excitation from $2p_{3/2}$ orbitals, whereas the higher-energy doublet (b_1 and b_2) corresponds to excitation from $2p_{1/2}$ orbitals. In each doublet, the major peak corresponds to a final state of the higher energy state in t_{2g} and e_g, while the lower one corresponds to the minor peak. The peak position differences a_2-a_1 and b_2-b_1 are determined by, but not identical to, $10Dq$ (de Groot et al. 1990). The leading peaks 1, 2, and b_{1o} are part of the multiplet spectrum and can be accounted for by the Coulomb repulsion and exchange terms (de Groot et al. 1990). In cubic coordination, the minor peak 2 occurs between the energies of the a_1 and a_2 peaks, which can be used to distinguish between cubic and octahedral coordination symmetries.

In a Ca $L_{2,3}$ NEXAFS spectrum, peak broadening is caused by the solid-state broadening effect when the sample becomes thicker and disorder appears in the crystal structures, which increases the number of inter-peak absorption states (Obst et al. 2009). The intensities of the minor peaks also increase more rapidly than those of the major peaks with increasing sample thickness. A previous study concluded that peak heights should not exceed 0.30 ± 0.05 optical density (OD) to obtain reliable spectra with no absorption saturation artifacts, corresponding to a sample thickness of 30 nm (Hanhan et al. 2009). However, conditions vary from beamline to beamline. Quantitative NEXAFS spectra with no saturation artifacts can be obtained using beamline 5.3.2.2 at the ALS of the Lawrence Berkeley National Laboratory for OD values of ~1.0, corresponding to a sample thickness of ~200 nm. Saturation effects are generally significant in the analysis of NEXAFS spectra of cement systems, as the typical grain size distribution in cement varies from ~100 nm to ~100 μm.

Materials and methods

To ensure purity, all samples studied here were lab-prepared phases, rather than from natural sources. Katoite, ettringite, C_3A_{cub}, and C_3A_{orth} powders were purchased from Mineral Research Processing (http://www.mineralresearchprocessing.fr/). The crystal structures and chemical compositions of these minerals were verified by powder X-ray diffraction (XRD) (Electronic Supplemental Material[1]). Gypsum was purchased from Fisher Scientific (no. S76764). Ca $L_{2,3}$-edge NEXAFS spectra of katoite, ettringite, C_3A_{cub}, and C_3A_{orth} were measured on samples prepared by drop-casting small amounts of these precursors directly onto Si_3N_4 windows. Ca

[1]Deposit item AM-17-45670, Supplemental Material. Deposit items are free to all readers and found on the MSA web site, via the specific issue's Table of Contents (go to http://www.minsocam.org/MSA/AmMin/TOC/2017/Apr2017_data/Apr2017_data.html).

$L_{2,3}$-edge NEXAFS spectra of kuzelite was obtained by spectromicroscopic analysis of samples produced by mixing gypsum, C_3A_{cub}, and deionized water by hand at a mass ratio of 0.4:1:14 in sealed plastic vials under ambient conditions (1 atm, 25 ± 2 °C). Small volumes (~0.2 µL) of the hydrated mixtures were drop-cast onto 100 nm thick Si_3N_4 windows (Norcada) after 9 days of reaction. The reactions were stopped by removing excess water immediately after drop-casting by gently contacting the mixtures with Kimwipes (Kimtech Science), leaving a thin layer of hydrated solids (Fig. 2) (Kilcoyne et al. 2003). Ca $L_{2,3}$-edge NEXAFS spectra of katoite and C_3A_{cub} were measured on samples prepared by drop-casting small amounts of these precursors directly onto Si_3N_4 windows.

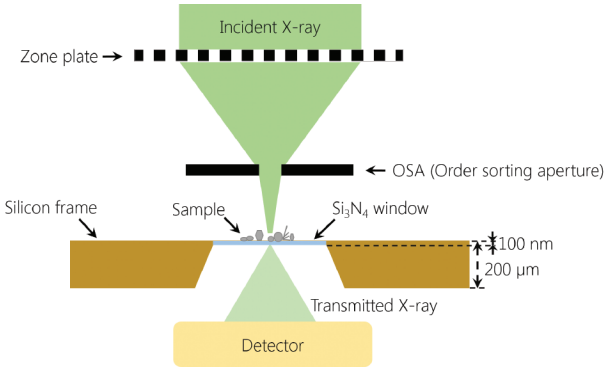

FIGURE 2. Schematic representation of a sample in the instrument chamber for Ca $L_{2,3}$-edge NEXAFS and STXM analysis (not to scale). (Color online.)

The STXM and Ca $L_{2,3}$-edge NEXAFS measurements were conducted at beamline 5.3.2.2 of the Advanced Light Source (Lawrence Berkeley National Laboratory), which operates at 1.9 GeV and 500 mA using a bending magnet source and an active servo-stabilized toroidal pre-mirror. Two computer-controlled slits are placed on each side of a low dispersion spherical grating monochromator. Within the energy range of 250–780 eV, the resolving power of the radiation source at beamline 5.3.2.2 is $E/\Delta E \sim 5000$ when using slit dimensions of approximately 20 × 10 × 10 µm and decreases to $E/\Delta E \sim 2000$ with slit dimensions of approximately 60 × 30 × 30 µm, where E is the incident beam energy and ΔE is the resolvable energy step size. The scanning transmission X-ray microscope installed on beamline 5.3.2.2 has a spatial scanning resolution limit of ~31 nm utilizing a 240 µm diameter zone plate, with the transmission signal recorded using a phosphor-coated photomultiplier tube (PMT) (Stöhr 2013; Collins and Ade 2012). The photon energy is calibrated by setting the position of the Rydberg 3*s* peak for CO_2 to 292.74 eV as detailed in reference (Collins and Ade 2012).

Samples were measured under 0.3 atm of helium. The energy scanning range was set to 340–360 eV, with a step size of 0.1 eV between 345 and 356 eV and a step size of 0.2 eV used at the other sampled energies. The measured data were processed using aXis2000 software (Hitchcock et al. 2012).

RESULTS AND DISCUSSION

Ca $L_{2,3}$-edge NEXAFS spectra and crystal chemistry

The Ca $L_{2,3}$-edge NEXAFS spectra of all the studied minerals show fine structures within the energy range of 346 to 354 eV (Fig. 3), consistent with Ca $L_{2,3}$-edge NEXAFS spectra of many Ca-containing minerals (Solomon et al. 2012; Ha et al. 2012; Jackson et al. 2013; Geng et al. 2015; Fleet and Liu 2009). Unique spectra were repeatedly observed for each mineral phase on different sampling regions of similar thickness, indicating that

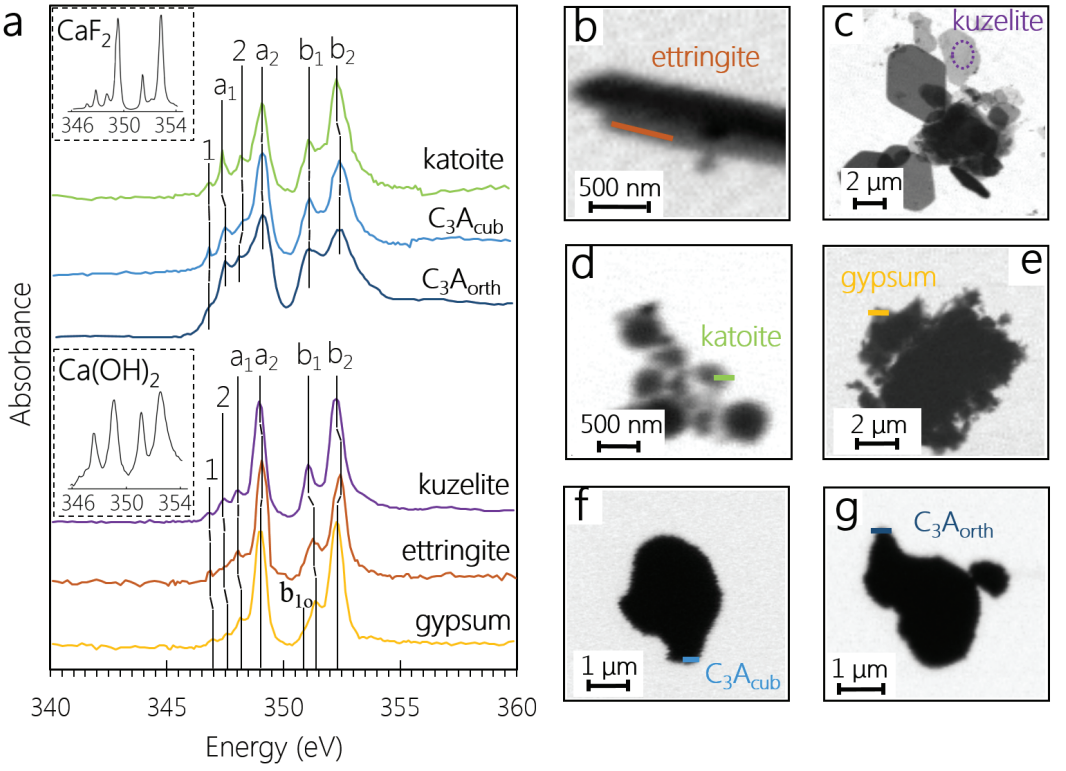

FIGURE 3. (**a**) Ca $L_{2,3}$-edge NEXAFS spectra of ettringite, kuzelite, katoite, gypsum, C_3A_{cub}, and C_3A_{orth}, collected from the regions in **b**–**g**. The absorption signals of the dashed circle or straight lines in each image were averaged to yield the spectra. Insets are spectra of CaF_2 (de Groot et al. 1990) and $Ca(OH)_2$ (Geng et al. 2015) as examples of cubic and octahedral coordination, respectively. (Color online.)

the chemical environment of Ca in each mineral is relatively homogeneous at the spatial resolution of ~30 nm.

Katoite. The shape of the Ca $L_{2,3}$-edge NEXAFS spectrum of katoite (Fig. 3) is similar to that of CaF_2 (de Groot et al. 1990; Naftel et al. 2001; Miedema et al. 2011), which contains Ca coordinated to eight F atoms in cubic symmetry. The cubic-like symmetry of katoite is confirmed by the larger peak energy differences of a_2-a_1 (1.70 eV) than b_2-b_1 (1.21 eV) in this phase. A similar a_2-a_1 energy difference is found for CaF_2 (1.60–1.70 eV), although the b_2-b_1 energy difference in CaF_2 (1.40–1.44 eV) is larger. According to Lager et al. (1987), all Ca and O atoms are in equivalent positions in katoite. Figure 4a shows that each Ca atom is coordinated to eight O atoms, half with Ca-O bond lengths of 2.360 Å and half with Ca-O bond lengths of 2.514 Å. Along the twofold rotation axis, the top four O atoms are labeled O_t and the bottom four are labeled O_b. The coordination symmetry of Ca in katoite is distorted from perfect cubic symmetry in two ways: (1) the different Ca-O bond lengths modify the positions of O atoms in the top and bottom planes of the structure to rectangular rather than square shapes; and (2) there is a slight misalignment of the top and bottom rectangles (Fig. 4a).

Ettringite. The Ca $L_{2,3}$-edge NEXAFS spectrum of ettringite (Fig. 3a) resembles that of octahedrally coordinated Ca both because the peak energy differences of a_2-a_1 and b_2-b_1 are comparable and because no peak is observed between a_1 and a_2. The leading peak 2 is almost indistinguishable in this spectrum. The energy differences between the peak positions a_2 and a_1 at the L_3 edge and b_2 and b_1 at the L_2 edge are 1.05 eV and 1.14 eV, respectively, which are low relative to the corresponding values for calcite and calcium hydroxide (Geng et al. 2015). The relatively low splittings of the L_3 and L_2 edges and low intensities of the minor a_1 and b_1 peaks indicate a weak crystal field.

So far three ettringite structures have been reported where Ca environments are highly comparable (Moore and Taylor 1970; Hartman and Berliner 2006; Goetz-Neunhoeffer and Neubauer 2006). Ettringite contains eightfold-coordinated Ca in two positions (Fig. 4b), with Ca-O bond lengths for Ca1 ranging from 2.356 to 2.739 Å, average of 2.464 Å, and those for Ca2 ranging from 2.317 to 2.747 Å, average of 2.491 Å (Moore and Taylor 1970). Viewing Ca1 along the (100) axis, the corners of the rectangle formed by two O1 atoms and two O3 atoms are misaligned with the corners of the rectangle formed by O6, O8, O10, and O12

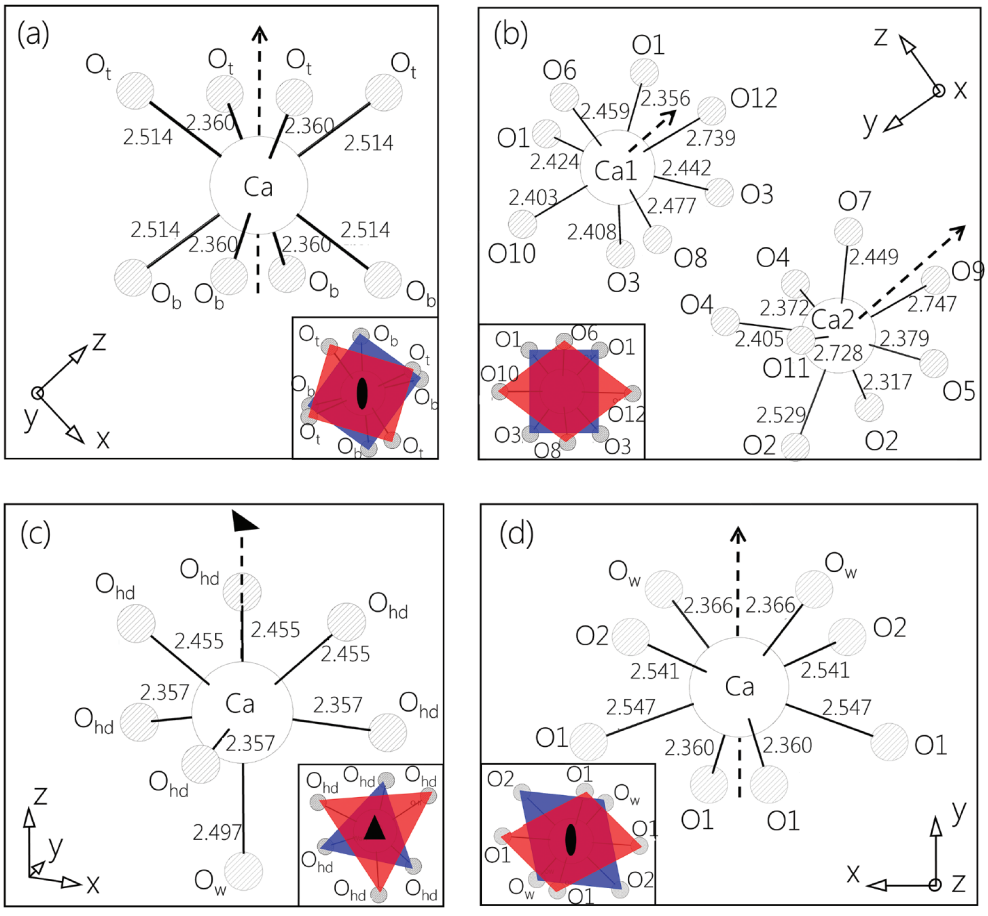

FIGURE 4. Coordination environments of Ca in (**a**) katoite (Lager et al. 1987), (**b**) ettringite (Moore and Taylor 1970), (**c**) kuzelite (Allmann 1977), and (**d**) gypsum (Comodi et al. 2008), with rotation axes marked by dashed lines. The insets show color blocks that illustrate the orientations of the roughly coplanar oxygen atoms viewed down the rotation axes. Filled ellipses and triangles represent twofold and threefold axes, respectively. Bond lengths are in angstroms. (Color online.)

atoms, and thus, the t_{2g} orbital is less destabilized by the ligands. Instead, the O8 atom and two O1 atoms can destabilize the d_{z^2} orbital from the axial direction and the five equatorial oxygen atoms, i.e., O6, O10, O12 and two O3 atoms can destabilize the $d_{x^2-y^2}$ and d_{xy} orbitals (note that O6 and O12 are slightly off the equatorial plane to the O8 side). In contrast, the d_{yz} and d_{xz} orbitals are less likely to be destabilized because their symmetry poorly matches that of the ligand configuration. Ca2 has a very similar configuration to Ca1, with O7 and O2 in axial positions and O5, O9, O11, O4s in equatorial positions. Based on the above reasoning, we predict that Ca in ettringite is in a weak crystal field with positive 10*Dq*. This matches very well with the Ca $L_{2,3}$-edge NEXAFS spectrum of ettringite in Figure 3a.

Kuzelite. The Ca $L_{2,3}$-edge NEXAFS spectra for kuzelite and ettringite are similar, except that the positions of the a_2, b_1, and b_2 peaks in the former phase are shifted to lower energy, which also has a relatively smaller L_3 splitting (0.93 eV) and a relatively larger L_2 splitting (1.18 eV). The Ca $L_{2,3}$-edge NEXAFS spectrum for kuzelite contains very well-resolved leading (1, 2) and minor (a_1, b_1) peaks and has a relatively high signal-to-noise ratio, which can be attributed to the analysis of large, uniformly thick and near-perfect hexagonal crystals (Fig. 3c).

In kuzelite, there is one equivalent Ca position (Allmann 1977) (Fig. 4c). The oxygen in water (O_w) is located on the (001) axis (threefold rotation axis) 2.497 Å from the central Ca atom; three hydroxyl O atoms in hydroxyl groups, labeled O_{hd}, are equatorially coordinated with bond lengths of 2.375 Å; another three O_{hd} atoms are coordinated to the central Ca atom from the opposite side of O_w with a bond length of 2.455 Å (referred as top O_{hd} atoms as viewed from the perspective shown in Fig. 4c, where the side that the rotation axis is pointing toward is denoted as the top side). There is a misalignment of 43.7° in the orientations of the equatorial O_{hd} regular triangle (blue triangle in Fig. 4c, inset) and the top O_{hd} regular triangle (red triangle in Fig. 4c, inset). In this configuration, only the d_{z^2} orbital is likely to be significantly destabilized, axially by O_w, on top by the O_{hd} triangle, and equatorially by the equatorial O_{hd} triangle. Compared with the strong destabilization of the perfect octahedral ligand configuration (Moore and Taylor 1970), we expect the Ca $L_{2,3}$-edge NEXAFS spectra for kuzelite to be similar to those with small positive 10*Dq*, which matches the result shown in Figure 3a.

Gypsum. The Ca $L_{2,3}$-edge NEXAFS spectrum measured for gypsum is similar to the spectra obtained for ettringite and kuzelite (Fig. 3a), although the L_3 edge peak splitting (a_2-a_1) of 0.85 eV and the L_2 edge peak splitting (b_2-b_1) of 0.90 eV for gypsum are smaller, indicating a weaker crystal field. Values of L_3 and L_2 edge splitting of ~0.95 eV have previously been reported for $CaSO_4$, indicating a stronger crystal field with emission of crystalliferous water (Patel and Aswath 2012). The Ca $L_{2,3}$-edge NEXAFS spectrum for gypsum also contains weak leading 1 and 2 peaks and shows a small, positive 10*Dq* value because peak 2 is located between peak 1 and a_1. There is an additional weak b_{1o} peak at 350.82 eV, which was not identified in the NEXAFS of perfectly octahedral coordinated compounds nor in theoretical calculations (de Groot et al. 1990). Therefore, the NEXAFS results for gypsum indicate that this phase contains Ca in distorted coordination symmetry with 3*d* orbitals destabilized in a way similar to octahedral coordination.

The analysis for gypsum presented above is consistent with the crystal chemistry of Ca in this phase (Comodi et al. 2008). In gypsum, Ca is coordinated to eight oxygen atoms in one equivalent position (Fig. 4d), with bond lengths ranging from 2.360 to 2.547 Å. The relative orientation of the two O2 atoms and two O_w atoms to the four O1 atoms in gypsum and katoite are similar if viewed along the (010) axis (i.e., the rotation axis), although neither the O2, O_w nor O1 atoms lie in the same plane. From the geometric point of view, the coordination of Ca in gypsum can be classified into neither octahedral-like nor cubic-like symme-

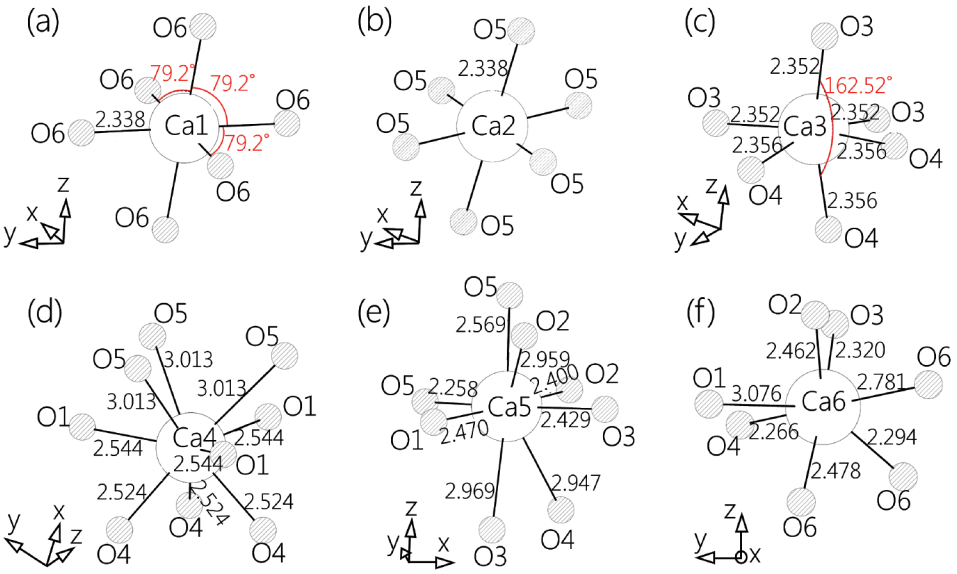

FIGURE 5. Coordination environments of the six Ca sites in the C_3A_{cub} unit cell (Mondal and Jeffery 1975): (**a**) Ca1; (**b**) Ca2; (**c**) Ca3; (**d**) Ca4; (**e**) Ca5; and (**f**) Ca6. Angles are marked with red labels. (Color online.)

try but rather a spherical-like symmetry, with 8 ligand O atoms distributing randomly within short range of distances from the center Ca. This leads to a much weaker splittings at the L_3 and L_2 edges than in ettringite and kuzelite.

Cubic and orthorhombic C_3A. The Ca $L_{2,3}$-edge NEXAFS spectrum C_3A_{cub} exhibits a cubic-like symmetry pattern with peak 2 located between the positions of peaks a_1 and a_2 with L_3 and L_2 edge splittings of 1.57 and 1.28 eV, respectively.

There are six Ca sites in the C_3A_{cub} unit cell (Mondal and Jeffery 1975) (Fig. 5). Ca1 and Ca2 have identical site symmetry and are in a distorted octahedral configuration with Ca-O bond lengths of 2.338 Å. All three oxygen pairs in Ca1 and Ca2 take Ca as the center, yet the angles between these pairs are 79.2° instead of 90°. Ca3 is also distorted from octahedral coordination with three 2.352 Å-long Ca-O bonds and three 2.356 Å-long Ca-O bonds. The angle of each O3-Ca-O4 bond is 162.52°. The four equatorial O atoms are not exactly coplanar. The coordination structures of Ca4, Ca5, and Ca6 are more complex, with Ca-O bond lengths varying between 2.258 and 3.013 Å. Therefore, Ca $L_{2,3}$-edge NEXAFS spectrum for C_3A_{cub} is a superposition of contributions from octahedrally coordinated Ca (Ca1, Ca2, and Ca3) and irregularly coordinated Ca (Ca4, Ca5, and Ca6) and is not expected to show strong L_2 and L_3 edge splitting because the percentage of octahedral-like sites is relatively low (11.1% for

TABLE 1. Numbers and locations of Ca and Na atoms in the C_3A_{cub} (Mondal and Jeffery 1975) and C_3A_{orth} unit cells (Nishi and Takeuchi 1975) (color online)

C_3A_{cub}	Number of atoms	Ca1 4	Ca2 4	Ca3 8	Ca4 8	Ca5 24	Ca6 24
	View from (–0.4, 0.7, 1.5)						
C_3A_{orth}	Number of atoms	Ca1 2 (occupancy 0.25)	Ca2 8	Ca3 8	Ca4 8	Ca5 8	Na 4
	View from (–1.5, 1, –0.24)						

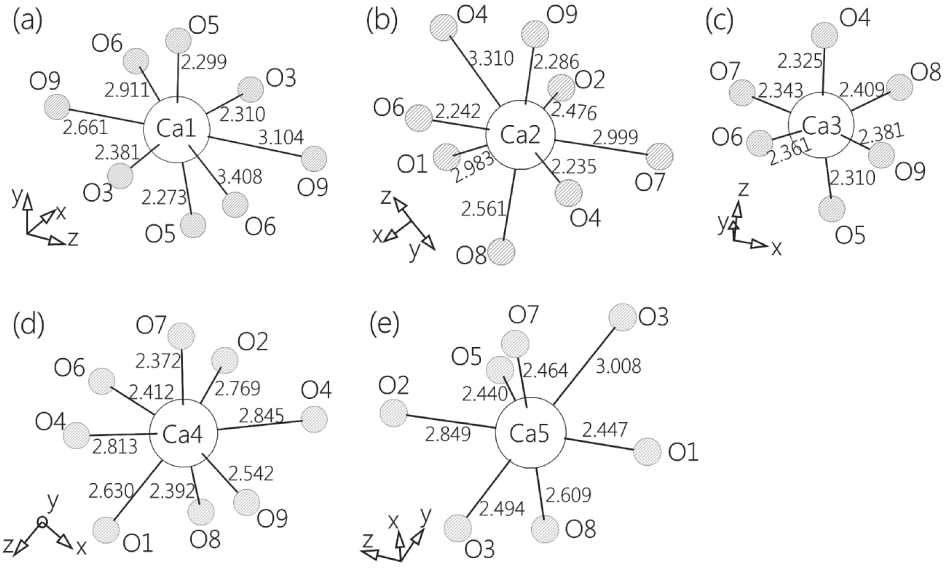

FIGURE 6. Coordination environments of the five Ca sites in the C_3A_{orth} unit cell (Nishi and Takeuchi 1975): (**a**) Ca1; (**b**) Ca2; (**c**) Ca3; (**d**) Ca4, and (**e**) Ca5.

summation of Ca1 and Ca2, 11.1% for Ca3, as shown in Table 1). The Ca $L_{2,3}$-edge NEXAFS spectrum for C_3A_{cub} is consistent with this line of reasoning, and the complex coordinations of Ca4, Ca5, and Ca6 produce cubic-like crystal field splitting effects with negative 10*Dq*.

The symmetry and size of the unit cell (Table 1) as well as the configurations of Ca atoms (Fig. 6) in C_3A_{orth} and C_3A_{cub} are different. In C_3A_{orth}, only Ca3 is in distorted octahedral coordination, with Ca-O bond lengths ranging from 2.31 to 2.409 Å (averaging at 2.355 Å). The other Ca atoms have irregular symmetries but higher coordination numbers (8 for Ca1, Ca2, and Ca4, and 7 for Ca5). Each of the eightfold-coordinated Ca atoms has four short Ca-O bonds (2.2–2.6 Å) and four long Ca-O bonds (2.6–3.5 Å), with average bond lengths of 2.668 Å for Ca1-O, 2.637 Å for Ca2-O, and 2.598 Å for Ca4-O. The Ca5 atom has four short Ca-O bonds (2.4–2.5 Å) and three long Ca-O bonds (2.6–3.1 Å), averaging 2.616 Å.

The previously mentioned symmetries of Ca atoms in C_3A_{orth} explains the cubic-like Ca $L_{2,3}$ edge NEXAFS spectrum that was measured for this phase (Fig. 3). This spectrum differs from that for C_3A_{cub} by a shift in the location of peak 2 to lower energy and a more broadened peak b_1, with otherwise minor differences in spectral line shape and peak positions. The energy differences between peaks a_2-a_1 and b_2-b_1 are slightly smaller in the Ca $L_{2,3}$ edge NEXAFS spectrum for C_3A_{orth} relative to C_3A_{cub}, indicating a slightly weaker crystal field of Ca in C_3A_{cub}. The doping of Na is not uniform on the unit-cell scale, leading to a fractional occupancy of Ca1, which breaks the perfect periodicity over long ranges (Nishi and Takeuchi 1975). This may explain the broadening of peak b_1 in the C_3A_{orth} spectrum. The sharpening of peak 2 in the spectrum of C_3A_{orth} could then be explained by the higher fraction of octahedral-like coordinated Ca3 atoms in C_3A_{orth} (23.5%) relative to C_3A_{cub} (11.1% for each of the two octahedral-like coordinated sites), whose a_1 peak is sharp (de Groot et al. 1990). Therefore, the Ca atoms in C_3A_{orth} are in cubic-like coordination with slightly weaker crystal fields than those in C_3A_{cub}.

Absorption saturation

In a transmission X-ray spectroscopy experiment, NEXAFS spectra become "saturated" once the sample thickness reaches a limiting value. Increasing sample thickness beyond this limit results in significantly broadened absorption peaks and increases the peak intensity ratio (PIR) of the minor peaks relative to the major peaks. The Ca $L_{2,3}$-edge NEXAFS spectra collected for ettringite, gypsum, and kuzelite samples of different thickness show that the PIRs of the leading and minor peaks typically increase with increasing sample thickness (Figs. 7 and 8b). Peaks 2 and b_{1o} in the Ca $L_{2,3}$-edge NEXAFS spectrum for gypsum, as well as peak 2 for ettringite, become increasingly difficult to resolve as the sample thickness increases. Most of the major peaks and some of the minor peaks in the Ca $L_{2,3}$-edge NEXAFS spectra for ettringite and gypsum become significantly broadened with increasing sample thickness, although the minor peaks (1, 2, a_1, a_2) in the Ca $L_{2,3}$-edge NEXAFS spectra for kuzelite do not display peak broadening. This is explained by the perfect or near-perfect crystal structure of the kuzelite crystallites sampled (Fig. 3c), such that relatively low amounts of structural-disorder-induced interpeak states are encountered for this phase. Unsurprisingly, peak positions remain unchanged during absorption saturation for all measured phases, meaning that individual phases in composite geochemical systems can be resolved by STXM using this parameter. The features located between 356 and 358 eV are artifacts caused by dynamic focusing of the zone plate.

Using maximum OD values to estimate sample thickness is a common approach (Hanhan et al. 2009). However, it could be impractical when the background absorption is comparable to the resonance absorption, which frequently occurs in thick sampling regions. Here, we propose another estimation of sample thickness. Sample thickness can be estimated using the Beer-Lambert Law (see Eqs. 1–2):

$$I = I_0\, e^{-\mu t} \quad (1)$$

$$\mathrm{OD} = \mu t = -\ln(I/I_0) \quad (2)$$

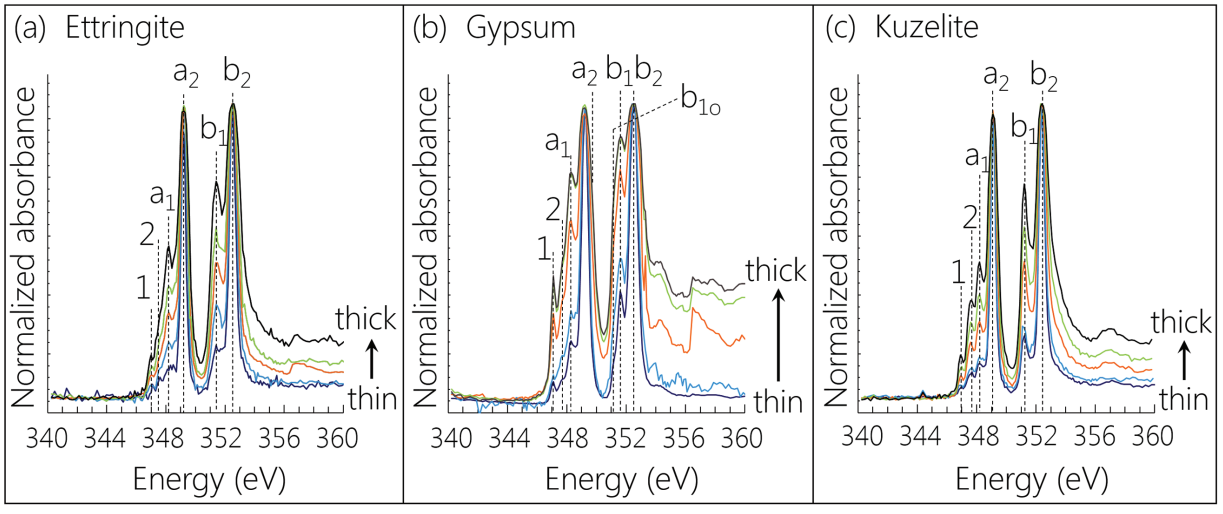

FIGURE 7. Ca $L_{2,3}$-edge NEXAFS spectra of (**a**) ettringite, (**b**) gypsum, and (**c**) kuzelite in samples of different thickness. The features located between 356 and 358 eV are measurement artifacts. (Color online.)

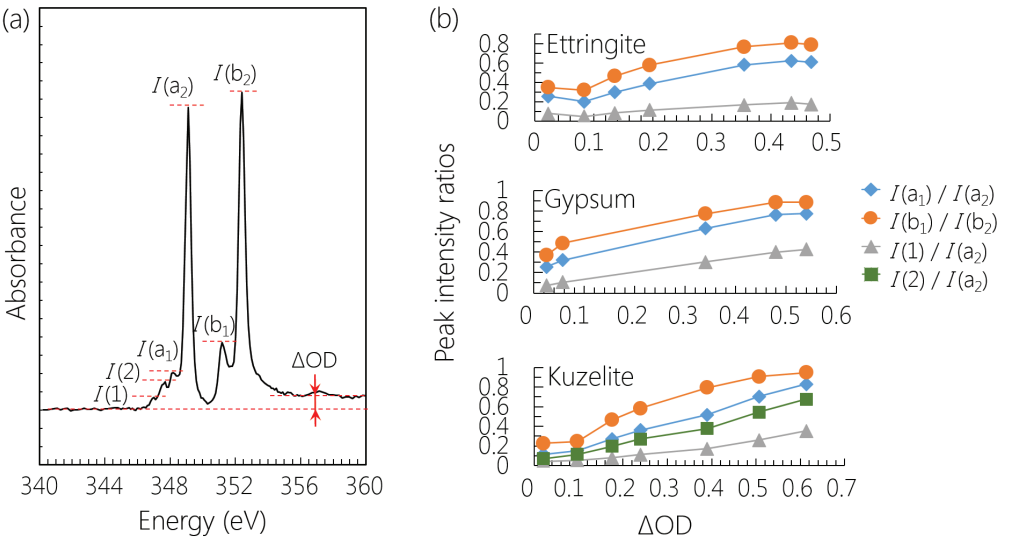

► **FIGURE 8.** (**a**) Sample thickness parameters indicated for a Ca $L_{2,3}$-edge NEXAFS spectrum of calcium monosulfoaluminate hydrate. (**b**) PIRs for ettringite, gypsum, and calcium monosulfoaluminate hydrate as functions of ΔOD. (Color online.)

where I_0 and I are the incident and transmitted beam intensities, respectively, t is the sample thickness, and μ is the attenuation coefficient (Hubbell and Seltzer 1995). Although μ is a function of the incident beam energy, it can be treated as a constant if the incident beam energy ranges within several tens of electron volts outside of an absorption edge (Fig. 8a). At the absorption edge, μ changes drastically with a small range of variation in beam energy. Beyond the absorption edge, μ once again changes immeasurably with beam energy, as illustrated in Figure 8a. The difference between the pre-edge and post-edge OD, i.e., the optical density difference (ΔOD), is related to t and Δμ, i.e., the difference in μ over this same energy range:

$$\Delta OD = \Delta \mu t \quad (3)$$

Values of minor to major PIRs in unnormalized Ca $L_{2,3}$-edge NEXAFS spectra with different ΔOD are shown in Figure 8b. Given the same ΔOD, the PIRs of ettringite, gypsum, and kuzelite are similar despite differences in attenuation coefficients and sample densities. For example, using $I(b_1)/I(b_2)$ at ΔOD = 0.4, the PIR of these minerals vary within the range 0.75–0.8. These results indicate that the ΔOD parameter may provide a universal measurement of sample attenuation thickness in STXM studies of heterogeneous microscale systems containing these phases.

The $I(b_1)/I(b_2)$ curve for kuzelite approaches its lower limit asymptotes at ΔOD < 0.1 and upper limit asymptotes at ΔOD ≥ 0.6. The same observation applies to all three curves of ettringite, where the lower limit is at ΔOD~0.08 and the upper limit is ΔOD~0.43. The $I(a_1)/I(a_2)$, $I(2)/I(a_2)$, and $I(1)/I(a_2)$ curves of kuzelite display only lower asymptotes at ΔOD < 0.1 because the ΔOD does not become large enough to cause full saturation in the minor peaks a_1, 1, and 2. For gypsum, a lower asymptote is not clear due to lack of sampling in the low ΔOD region but an upper asymptote is obtained for ΔOD > 0.5. In the medium OD range (approximately 0.1~0.4), the slope of all PIR curves for these phases increase approximately linearly.

IMPLICATIONS

Our work has implications for cement chemistry, in demonstrating novel methods to investigate unsolved topics, such as the retardation mechanism of calcium sulfate (hydrates) on the otherwise rapid hydration of C_3A, which is critical to understanding the early age performance of fresh concrete mixtures. Another potential application lies in the hydration dynamics of calcium sulfoaluminate cement, which is a promising alternative to ordinary Portland cement that may reduce the heavy carbon footprint of the cement industry (Justnes 2012). Clearly, STXM can be a powerful chemical and morphological probe to study rapidly evolving aqueous systems, given that the reference spectra are well resolved.

ACKNOWLEDGMENTS

Guoqing Geng's research at the University of California, Berkeley, is supported by the Chinese Scholarship Council (file no. 201206090127). The authors acknowledge the financial support received from Siam Cement, Thailand. The Advanced Light Source is supported by the Director, Office of Science, Office of Basic Energy Sciences, of the U.S. Department of Energy under Contract No. DE-AC02-05CH11231.

REFERENCES CITED

Albright, T.A., Burdett, J.K., and Whangbo, M.H. (2013) Orbital Interactions in Chemistry. Wiley.
Allmann, R. (1977) Refinement of the hybrid layer structure $[Ca_2Al(OH)_6]^+ \cdot [1/2SO_4 \cdot 3H_2O]^-$. Neues Jahrbych für Mineralogie Monatshefte, 136–144.
Barnes, P., and Bensted, J. (2002) Structure and Performance of Cements. CRC Press.
Baur, I., and Johnson, C.A. (2003) Sorption of selenite and selenate to cement minerals. Environmental Science & Technology, 37(15), 3442–3447.
Bell, D.R., and Rossman, G.R. (1992) Water in Earth's mantle: the role of nominally anhydrous minerals. Science, 255, 1391.
Black, L., Garbev, K., Stemmermann, P., Hallam, K.R., and Allen, G.C. (2003) Characterisation of crystalline CSH phases by X-ray photoelectron spectroscopy. Cement and Concrete Research, 33(6), 899–911.
Burns, R.G. (1993) Mineralogical applications of crystal field theory (Vol. 5). Cambridge University Press.
Chen, C., Dynes, J.J., Wang, J., Karunakaran, C., and Sparks, D.L. (2014) Soft X-ray spectromicroscopy study of mineral-organic matter associations in pasture soil clay fractions. Environmental Science & Technology, 48(12), 6678–6686.
Chrysochoou, M., and Dermatas, D. (2006) Evaluation of ettringite and hydrocalumite formation for heavy metal immobilization: literature review and

experimental study. Journal of Hazardous Materials, 136(1), 20–33.
Collins, B.A., and Ade, H. (2012) Quantitative compositional analysis of organic thin films using transmission NEXAFS spectroscopy in an X-ray microscope. Journal of Electron Spectroscopy and Related Phenomena, 185(5), 119–128.
Comodi, P., Nazzareni, S., Zanazzi, P.F., and Speziale, S. (2008) High-pressure behavior of gypsum: a single-crystal X-ray study. American Mineralogist, 93, 1530–1537.
Davidovits, J. (1994) Properties of geopolymer cements. In First International Conference on Alkaline Cements and Concretes, 1, p. 131–149. Scientific Research Institute on Binders and Materials, Kiev State Technical University, Ukraine.
de Groot, F.M.F., Fuggle, J.C., Thole, B.T., and Sawatzky, G.A. (1990) $L_{2,3}$ X-ray-absorption edges of d^0 compounds: K^+, Ca^{2+}, Sc^{3+}, and Ti^{4+} in Oh (octahedral) symmetry. Physical Review B, 41(2), 928.
Fleet, M.E., and Liu, X. (2009) Calcium $L_{2,3}$-edge XANES of carbonates, carbonate apatite, and oldhamite (CaS). American Mineralogist, 94, 1235–1241.
Geng, G., Taylor, R., Bae, S., Hernández-Cruz, D., Kilcoyne, D.A., Emwas, A.H., and Monteiro, P.J. (2015) Atomic and nano-scale characterization of a 50-year-old hydrated C_3S paste. Cement and Concrete Research, 77, 36–46.
Goetz-Neunhoeffer, F., and Neubauer, J. (2006) Refined ettringite ($Ca_6Al_2(SO_4)_3(OH)_{12}\cdot 26H_2O$) structure for quantitative X-ray diffraction analysis. Powder Diffraction, 21(01), 4–11.
Ha, J., Chae, S., Chou, K.W., Tyliszczak, T., and Monteiro, P.J.M. (2012) Effect of polymers on the nanostructure and on the carbonation of calcium silicate hydrates: a scanning transmission X-ray microscopy study. Journal of Materials Science, 47(2), 976–989.
Hanhan, S., Smith, A.M., Obst, M., and Hitchcock, A.P. (2009) Optimization of analysis of soft X-ray spectromicroscopy at the Ca 2p edge. Journal of Electron Spectroscopy and Related Phenomena, 173(1), 44–49.
Hartman, M.R., and Berliner, R. (2006) Investigation of the structure of ettringite by time-of-flight neutron powder diffraction techniques. Cement and Concrete Research, 36(2), 364–370.
Hashem, F.S., and Amin, M.S. (2014) Kinetic and thermal studies of removal of CrO_4^{2-} ions by ettringite. Journal of Thermal Analysis and Calorimetry, 116(2), 835–844.
Hillier, S., Lumsdon, D.G., Brydson, R., and Paterson, E. (2007) Katoite: A host phase for Cr (VI) in chromite ore processing residue (COPR) and other high pH wastes. Environmental Science & Technology, 41(6), 1921–1927.
Hitchcock, A.P., Hitchcock, P., Jacobsen, C., Zimba, C., Loo, B., Rotenberg, E., Denlinger, J., and Kneedler. R. (2012) aXis 2000—Analysis of X-ray Images and Spectra. McMaster University, Hamilton.
Hubbell, J.H., and Seltzer, S.M. (1995) Tables of X-ray mass attenuation coefficients and mass energy-absorption coefficients 1 keV to 20 MeV for elements z = 1 to 92 and 48 additional substances of dosimetric interest (no. PB-95-220539/XAB; NISTIR-5632). Ionizing Radiation Division, National Institute of Standards and Technology-PL, Gaithersburg, Maryland.
Jackson, M.D., Chae, S.R., Mulcahy, S.R., Meral, C., Taylor, R., Li, P., Emwas, A.H., Moon, J., Yoon, S., Vola, G., Wenk, H.R., and Monteiro. P.J.M. (2013) Unlocking the secrets of Al-tobermorite in Roman seawater concrete. American Mineralogist, 98, 1669–1687.
Justnes, H. (2012) Alternative low-CO_2 "green" clinkering process. Reviews in Mineralogy and Geochemistry, 74(1), 83–89.
Kilcoyne, A.L.D., Tyliszczak, T., Steele, W.F., Fakra, S., Hitchcock, P., Franck, K., Anderson, E., Harteneck, B., Rightor, E.G., Mitchell, G.E., and Hitchcock, A.P. (2003) Interferometer-controlled scanning transmission X-ray microscopes at the Advanced Light Source. Journal of Synchrotron Radiation, 10(2), 125–136.
Lager, G.A., Armbruster, T., and Faber, J. (1987) Neutron and X-ray diffraction study of katoite $Ca_3Al_2(O_4H_4)_3$. American Mineralogist, 72, 756–765.
McNeill, C.R., Watts, B., Swaraj, S., Ade, H., Thomsen, L., Belcher, W., and Dastoor, P.C. (2008) Evolution of the nanomorphology of photovoltaic polyfluorene blends: sub-100 nm resolution with X-ray spectromicroscopy. Nanotechnology, 19(42), 424015.
Mehta, P.K., and Monteiro, P.J.M. (2014) Concrete: Microstructure, Properties, and Materials, 4th edition. McGraw-Hill, New York.
Miedema, P.S., Ikeno, H., and de Groot, F.D. (2011) First principles multiplet calculations of the calcium $L_{2,3}$ X-ray absorption spectra of CaO and CaF_2. Journal of Physics: Condensed Matter, 23(14), 145501.
Mondal, P., and Jeffery, J.W. (1975) The crystal structure of tricalcium aluminate, $Ca_3Al_2O_6$. Acta Crystallographica, B31(3), 689–697.
Moore, A.E., and Taylor, H.F.W. (1970) Crystal structure of ettringite. Acta Crystallographica, B26(4), 386–393.
Naftel, S.J., Sham, T.K., Yiu, Y.M., and Yates, B.W. (2001) Calcium L-edge XANES study of some calcium compounds. Journal of Synchrotron Radiation, 8(2), 255–257.
Nelson, R.E. (1982) Carbonate and gypsum. Methods of Soil Analysis. Part 2. Chemical and Microbiological Properties, 181–197.
Nishi, F., and Takeuchi, Y. (1975) The $A_{16}O_{18}$ rings of tetrahedra in the structure of $Ca_{8.5}NaAl_6O_{18}$. Acta Crystallographica, B31(4), 1169–1173.
Obst, M., Dynes, J.J., Lawrence, J.R., Swerhone, G.D.W., Benzerara, K., Karunakaran, C., Kaznatcheev, K., Tyliszczak, T., and Hitchcock, A.P. (2009) Precipitation of amorphous $CaCO_3$ (aragonite-like) by cyanobacteria: a STXM study of the influence of EPS on the nucleation process. Geochimica et Cosmochimica Acta, 73(14), 4180–4198.
Patel, M., and Aswath, P.B. (2012) Morphology, structure and chemistry of extracted diesel soot: part II: X-ray absorption near edge structure (XANES) spectroscopy and high resolution transmission electron microscopy. Tribology International, 52, 17–28.
Puppala, A.J., Intharasombat, N., and Vempati, R.K. (2005) Experimental studies on ettringite-induced heaving in soils. Journal of Geotechnical and Geoenvironmental Engineering, 131, 325–337.
Sandford, S.A., Aléon, J., Alexander, C.M.D., Araki, T., Bajt, S., Baratta, G.A., Borg, J., Bradley, J.P., Brownlee, D.E., Brucato, J.R., and Burchell, M.J. (2006) Organics captured from comet 81P/Wild 2 by the Stardust spacecraft. Science, 314, 1720–1724.
Sasaki, T., Atsushi, I., Masayuki, W., Teruhisa, H., and Akihiro, Y. (2014) Preparation and performance of arsenate (V) adsorbents derived from concrete wastes. Waste Management, 34(10), 1829–1835.
Skibsted, J., Henderson, E., and Jakobsen, H.J. (1993) Characterization of calcium aluminate phases in cements by aluminum-27 MAS NMR spectroscopy. Inorganic Chemistry, 32(6), 1013–1027.
Solomon, D., Lehmann, J., Harden, J., Wang, J., Kinyangi, J., Heymann, K., Karunakaran, C., Lu, Y., Wirick, S., and Jacobsen, C. (2012) Micro-and nano-environments of carbon sequestration: Multi-element STXM-NEXAFS spectromicroscopy assessment of microbial carbon and mineral associations. Chemical Geology, 329, 53–73.
Stöhr, J. (2013) NEXAFS Spectroscopy (vol. 25). Springer Science & Business Media.
Taylor, H.F.W. (1997) Cement Chemistry, 2nd ed. Thomas Telford, London.
van Aardt, J.H., and Visser, S. (1977) Formation of katoites: calcium hydroxide attack on clays and feldspars. Cement and Concrete Research, 7(1), 39–44.
Wan, J., Tyliszczak, T., and Tokunaga, T.K. (2007) Organic carbon distribution, speciation, and elemental correlations within soil microaggregates: applications of STXM and NEXAFS spectroscopy. Geochimica et Cosmochimica Acta, 71(22), 5439–5449.
Warwick, T., Ade, H., Kilcoyne, D., Kritscher, M., Tyliszczak, T., Fakra, S., Hitchcock, A., Hitchcock, P., and Padmore, H. (2002) A new bend-magnet beamline for scanning transmission X-ray microscopy at the Advanced Light Source. Journal of Synchrotron Radiation, 9(4), 254–257.
Zhou, Q., Milestone, N.B., and Hayes, M. (2006) An alternative to Portland cement for waste encapsulation—the calcium sulfoaluminate cement system. Journal of Hazardous Materials, 136(1), 120–129.

Manuscript received December 2, 2015
Manuscript accepted November 29, 2016
Manuscript handled by Maarten Broekmans